

Comparison of time profiles for the magnetic transport of cold atoms

T. Badr,^{1,2} D. Ben Ali,^{2,1} J. Seaward,^{2,1} Y. Guo,^{2,1} F. Wiotte,^{2,1} R. Dubessy,^{2,1} H. Perrin,^{1,2} and A. Perrin^{1,2}

¹*CNRS, UMR7538, F-93430, Villetaneuse, France*

²*Université Paris 13, Sorbonne Paris Cité, Laboratoire de physique des lasers, F-93430, Villetaneuse, France*

(Dated: April 30, 2019)

We have compared different time profiles for the trajectory of the centre of a quadrupole magnetic trap designed for the transport of cold sodium atoms. Our experimental observations show that a smooth profile characterized by an analytical expression involving the error function minimizes the transport duration while limiting atom losses and heating of the trapped gas. Using numerical calculations of single atom classical trajectories within the trap, we show that this observation can be qualitatively interpreted as a trade-off between two types of losses: finite depth of the confinement and Majorana spin flips.

I. INTRODUCTION

The transport of cold atoms over macroscopic distances is now a well established technique that allows one to spatially isolate two stages in the production of degenerate quantum gases [1]; typically a cold sample is prepared in a magneto-optical trap (MOT) in a first vacuum chamber, and conveyed to a second one with a lower background pressure for a final evaporation stage. This, for instance, gives the opportunity to improve optical and mechanical access where the atoms are manipulated and observed. This can also allow for an increase of the repetition rate of the experiments, with the MOT being loaded while the final part of the experimental sequence is performed.

Various implementations have been explored involving either magnetic or optical fields: a chip magnetic conveyor belt [2, 3], time-varying currents in an assembly of anti-Helmholtz coils [1, 4], optical tweezers [5–7], a single pair of anti-Helmholtz coils on a translation stage [8, 9], a train of Ioffe-Pritchard traps [10] or a unidimensional optical lattice [11]. Recently, optimal control has been applied in harmonic [12] and anharmonic potentials [13, 14]. These works allow for the design of fast transport trajectories going far beyond the adiabaticity criterion. In linear traps, the possibility of Majorana spin flips [15] prevents from the existence of adiabatic trajectories which motivates other approaches.

The main objective of this paper is to compare different time profiles for the trajectory of a quadrupole magnetic trap centre and attempt to identify the main factors explaining their performances. In section II, we recall the basic principles of magnetically trapping cold atoms in a quadrupole magnetic trap and we give details on the experimental design we have used to transport cold atomic gases. In section III we investigate different time profiles for the trap centre motion and present our experimental observations. In order to understand our results, we have performed simulations of classical trajectories of the atoms within the moving quadrupole trap. Comparing different time profiles, we propose a qualitative explanation of our experimental results in section IV. Finally, section V gives concluding remarks.

II. EXPERIMENTAL IMPLEMENTATION

A. Basic principles

A straightforward realization of a quadrupole trap can be experimentally obtained with two identical coils in an anti-Helmholtz configuration, e.g. separated along their axis of revolution by a distance comparable to their radii and carrying the same current, I , flowing in opposite directions. At the symmetry center of the assembly, O , the produced magnetic field \mathbf{B} vanishes and can be approximated close to this position by a quadrupole field. Assuming z is the axis of revolution of the assembly, it reads

$$\mathbf{B}(x, y, z) \simeq \begin{pmatrix} -b'x \\ -b'y \\ 2b'z \end{pmatrix} \quad (1)$$

where b' is the magnetic field gradient. The latter depends on the exact geometry of the coils and is proportional to I [16].

A set of two pairs of anti-Helmholtz coils with z -axis separated along the y -axis by a distance comparable to their radii also produces a quadrupole field at a position $(0, y_0, 0)$ entirely determined by the currents flowing in each pair of coils. Close to $(0, y_0, 0)$, the resulting magnetic field \mathbf{B} reads

$$\mathbf{B}(x, y, z) \simeq 2b' \begin{pmatrix} -\frac{\alpha}{1+\alpha}x \\ -\frac{1}{1+\alpha}(y - y_0) \\ z \end{pmatrix} \quad (2)$$

where α is defined as the ratio of magnetic gradients along the x - and y -axis.

An atom with magnetic moment μ interacts with the magnetic field leading to a coupling V . For ^{23}Na atoms in their ground state, $3^2S_{1/2}$ as considered here, as long as V remains small compared to the hyperfine splittings, one can write

$$V(x, y, z) \simeq 2g_F m_F \mu_B b' \sqrt{\frac{\alpha^2 x^2}{(1+\alpha)^2} + \frac{(y - y_0)^2}{(1+\alpha)^2} + z^2} \quad (3)$$

where g_F is the Landé factor in the ground state F , μ_B the Bohr magneton and m_F the atomic spin projection onto local direction of the magnetic field. As soon as $g_F m_F > 0$, V presents a minimum where atoms can be confined. In the following, we neglect gravity since the magnetic gradients b' considered here are sufficiently large.

A minimum of three free parameters are necessary to control the values of y_0 , α and b' . With two sets of anti-Helmholtz coils, only two currents can be freely and independently tuned. Therefore, it is not possible to move the quadrupole trap along the (Oy) axis while keeping both α and b' constant [1]. Adding a third pair of anti-Helmholtz coils along the (Oy) axis offers an additional degree of freedom which lifts this constraint while keeping the same shape for the magnetic field, \mathbf{B} , as in Eq. 2.

Overall, the experimental design of a magnetic transport of cold atoms in a quadrupole trap relying on static anti-Helmholtz coils requires a minimum of three independent current supplies. In practice, additional experimental constraints may limit the control over the trap parameters y_0 , α and b' . For instance, if the current supplies are not bipolar, the range of accessible values for α gets restricted to values typically larger than 1.5. Moreover, switching smoothly from one set of three pairs of anti-Helmholtz coils to the next requires going through a configuration where only two current supplies out of three deliver a non-zero current. In turn, at these switching positions, only α or b' but not both can be freely set.

B. Experimental design

Our magnetic transport design is inspired by [4]. It relies on 15 pairs of anti-Helmholtz coils and an additional so-called push coil (see Fig. 1). It allows for transport of atoms along two stages of orthogonal direction and of length $L_1 = 30.7$ cm and $L_2 = 34.4$ cm respectively. The atoms are initially confined into a magneto-optical trap (MOT) [17] before being transferred into a quadrupole magnetic trap involving only the MOT coils. During the process, b' is ramped up to 65 G/cm and the atoms eventually occupying the $|F = 1, m_F = -1\rangle$ Zeeman substate are trapped. At the end of the magnetic transport, the atoms are ready to be transferred onto an atom chip.

Determining the value of the currents passing through the different coils along the first stage of the magnetic transport requires setting the dependence of α and b' on y_0 . We have chosen to keep $b' = 65$ G/cm constant throughout the magnetic transport. The value of α is equal to one at the beginning and at the end of the first stage, where a single pair of anti-Helmholtz coils is used and the atomic cloud is at rest. As mentioned in the previous section, since we rely on only three non-bipolar current supplies, the value of α is also constrained at each switching position between different sets of three pairs of anti-Helmholtz coils. We explain in appendix B how to determine these positions. The value of α is lin-

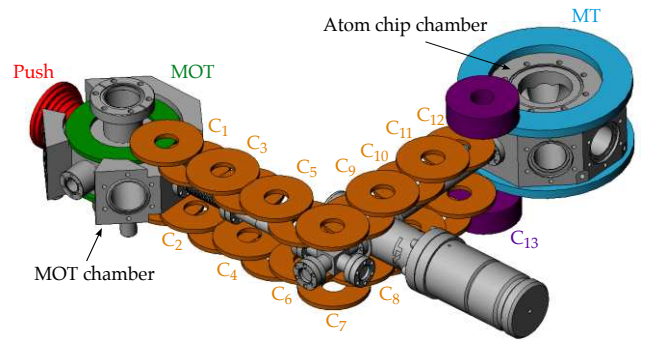


FIG. 1. Overview of the magnetic transport design which connects the MOT chamber to the atom chip chamber. It consists in 15 pairs of anti-Helmholtz coils: MOT, C_1 to C_{13} and MT. An additional push coil is used to produce a magnetic gradient which allows to control the geometry of the quadrupole magnetic trap at the beginning of the transport.

early interpolated between these spots apart from the last part of the first stage where only two pairs of anti-Helmholtz coils are then available (C_6 and C_7) and therefore α evolves freely. This is also the case at the beginning (C_7 and C_8) and end (C_{13} and MT) of the second stage.

Relying on the analytical formula of the magnetic field induced by a single current loop [16] and neglecting the helicity of the coils, it is straightforward to obtain an analytical formula for V which takes into account the geometry of each coil and includes their respective number of windings. At each position y_0 we then fit the magnetic gradients and set the currents so that V fulfills our requirements for α and b' . The results are shown in Fig. 2. The relative accuracy of the fit on y_0 , α and b' after this procedure is better than 0.1%. Additional technical details are given in appendix B. The same method is used for the second stage of the magnetic transport.

III. TIME PROFILES COMPARISON

A. Overview

Controlled displacement of the magnetic trap requires defining the dependence of y_0 on the time t . One of the simplest solution consists in following a constant velocity trajectory:

$$\begin{aligned} y_0(t) &= 0 & t \leq 0 \\ y_0(t) &= L_1 \frac{t}{\Delta t} & 0 < t < \Delta t \\ y_0(t) &= L_1 & t \geq \Delta t \end{aligned} \quad (4)$$

where Δt is the duration of the one-way magnetic transport from the MOT chamber to C_7 . In this case the acceleration of the trap center diverges at $t = 0$ and $t = \Delta t$ since the velocity is discontinuous. Outside these two

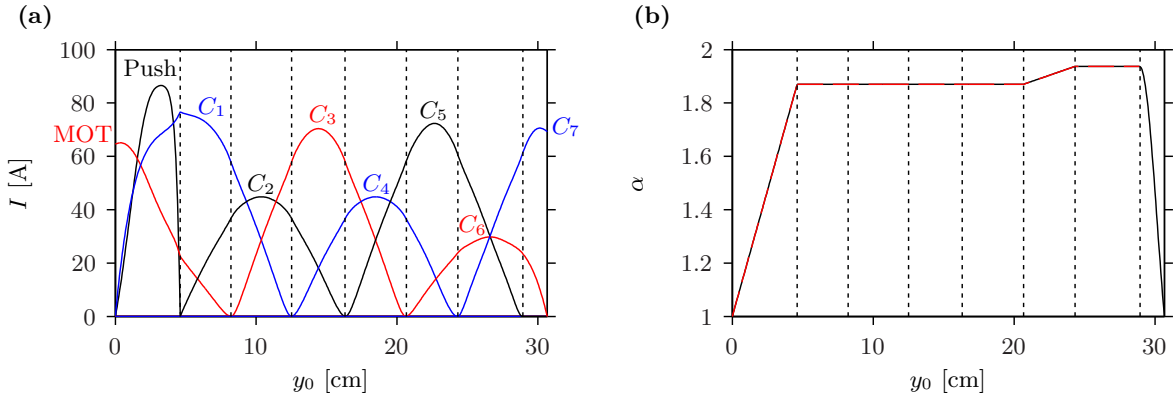


FIG. 2. (a) Currents in the different coils along the first stage of the magnetic transport. Each color corresponds to one of the current supplies. (b) Fitted value of the horizontal trap isotropy ratio, α , along the first stage of the magnetic transport (black line). The red dashed line shows the fit target for α (see Appendix B for details). In (a) and (b), the black dotted vertical lines indicate the switching position between two consecutive sets of three pairs of anti-Helmholtz coils.

points, the effective potential for the atoms in the comoving frame is the same as in the lab frame.

Another obvious possibility is a constant acceleration trajectory

$$\begin{aligned} y_0(t) &= 0 \quad t \leq 0 \\ y_0(t) &= 2L_1 \left(\frac{t}{\Delta t} \right)^2 \quad 0 < t \leq \frac{\Delta t}{2} \\ y_0(t) &= L_1 \left[1 - 2 \left(1 - \frac{t}{\Delta t} \right)^2 \right] \quad \frac{\Delta t}{2} < t < \Delta t \\ y_0(t) &= L_1 \quad t \geq \Delta t. \end{aligned} \quad (5)$$

In this case the velocity of the trap center is continuous while the acceleration is not. The effective potential for the atoms in the comoving frame gets tilted so that its gradient along the (Oy) axis is $\mp 2g_F m_F \mu_B b' / (1 + \alpha) + 4mL_1 / \Delta t^2$ for $y < y_0(t)$ and $y > y_0(t)$ respectively with $t \in [0, \Delta t/2]$. This is the opposite for $t \in [\Delta t/2, \Delta t]$, which implies an abrupt change in the tilt of the potential in the middle of the trajectory.

Countless other trajectories are conceivable. A few extra examples are given in appendix C. We will focus in the following on a family of trajectories which give good results experimentally. It relies on the error function:

$$\begin{aligned} y_0(t) &= 0 \quad t \leq 0 \\ y_0(t) &= \frac{L_1}{2} \left\{ 1 + \operatorname{erf} \left[-\gamma \left(\frac{t}{\Delta t} \right)^{-\delta} + \gamma \left(1 - \frac{t}{\Delta t} \right)^{-\delta} \right] \right\} \quad 0 < t < \Delta t \\ y_0(t) &= L_1 \quad t \geq \Delta t \end{aligned} \quad (6)$$

where $\delta > 0$ and $\gamma = 2^{-3/2-\delta} \sqrt{(\delta+1)(\delta+2)} / \delta$ ensures that the jerk of the trap center at $\Delta t/2$ vanishes. This allows the acceleration to be close to zero for a large portion of L_1 . This trajectory is extremely smooth, with continuous derivatives at all orders. The potential in the

comoving frame is only tilted at the beginning and end of the trajectory.

Figure 3 shows the behaviour of the position (a), velocity (b) and acceleration (c) of the trap center for different time profiles. Slight changes in the trajectory can result in large modifications of the acceleration. When the absolute value of the latter becomes larger than $2g_F m_F \mu_B b' / [(1 + \alpha)m]$, the potential V in the comoving frame gets tilted enough so that the atoms are not trapped anymore. This sets a limit on Δt above which the atoms remain confined throughout the magnetic transport. This is illustrated in Fig. 3(d) for the different time profiles considered here. For our typical magnetic gradients and $\alpha \simeq 2$ we see that Δt must be at least larger than 300 ms for the error function time profile.

It is important to note that experimentally, the bandwidth of the current supplies is finite which may filter the current output profiles and affect the magnetic transport sequence. We have checked that this effect is negligible in the different situations we have studied.

B. Experimental results

We have experimentally compared the number of atoms remaining in the magnetic trap after a round trip along the first stage of the magnetic transport for different time profiles and different Δt . The time profile is just reversed on the way back without any waiting time at the end. In order to account for the losses due to the finite lifetime of the atoms in the trap (about 15 s), we have normalized the results by the number of atoms remaining in the magnetic trap after the same total duration, $2\Delta t$, but without moving; this leads to the ratio r_N^2 . Fig. 4(a) shows that the error function time profile allows us to keep a maximum of about 75% of the atoms after the round trip and for shorter Δt than any other time profile. The worst results are obtained with

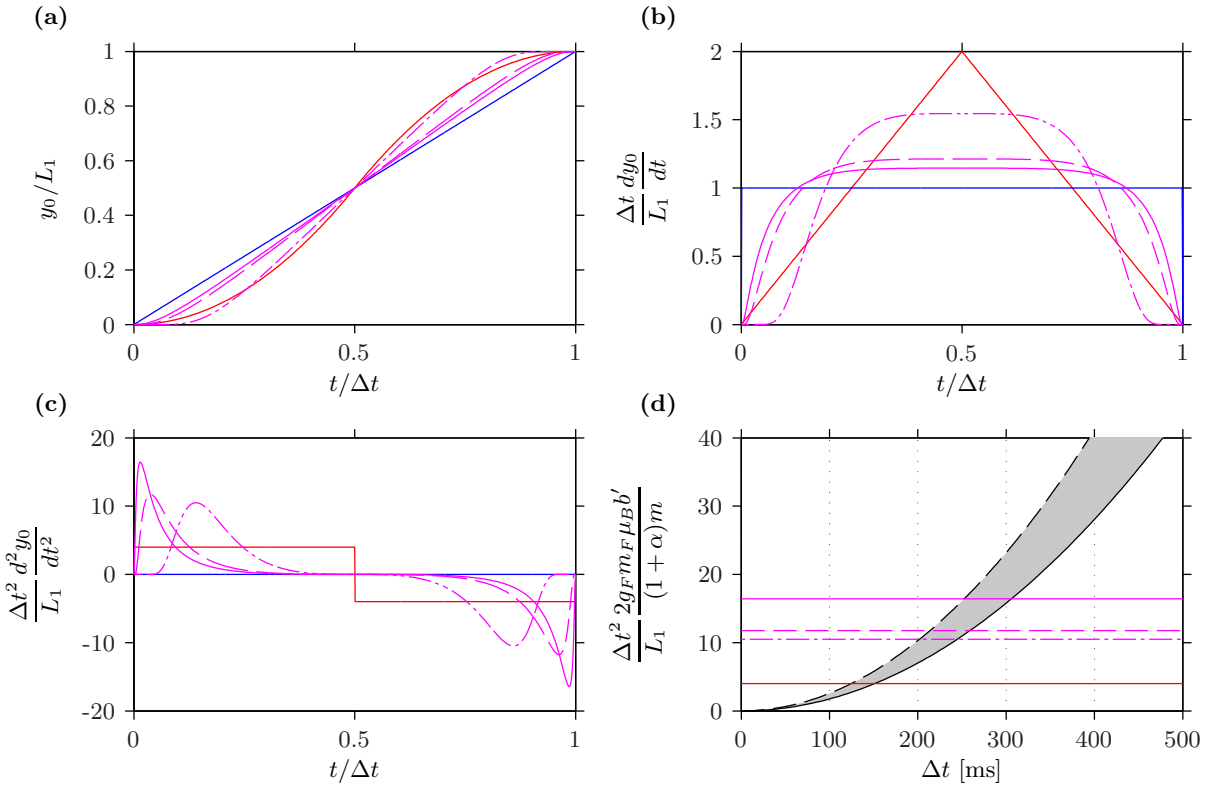


FIG. 3. (a) Behaviour of y_0 for different time profiles: constant velocity (blue solid line), constant acceleration (red solid line), error function shape (magenta lines) : $\delta = 0.02$ (solid), $\delta = 0.1$ (dashed) and $\delta = 0.5$ (dashed-dotted). (b) Same as (a) for the velocity of the trap center. (c) Same as (a) for the acceleration of the trap center. (d) Absolute value of the acceleration corresponding to the slope of the potential V in units of $L_1/\Delta t^2$: $b' = 65$ G/cm and $\alpha = 1.937$ (black solid line) and $\alpha = 1$ (black dashed line). The grey shaded area indicates the range of slopes covered during the trajectory. The three horizontal magenta lines correspond to the maximal absolute value of the acceleration in units of $L_1/\Delta t^2$ of the error function time profiles: $\delta = 0.02$ (solid line), $\delta = 0.1$ (dashed line) and $\delta = 0.5$ (dashed-dotted line). The horizontal red line is the same for the constant acceleration profile.

constant velocity time profile while constant acceleration time profile gives intermediate results.

We have also compared the results of the error function time profile for different δ . The results are shown in Fig. 4(b). The best results are obtained for the lowest value of δ . Note that $\delta = 0$ corresponds to the following trap center trajectory

$$y_0(t) = \begin{cases} 0 & t \leq 0 \\ \frac{L_1}{2} \left\{ 1 - \text{erf} \left[\log \left(\sqrt{\frac{\Delta t - t}{t}} \right) \right] \right\} & 0 < t < \Delta t \\ L_1 & t \geq \Delta t. \end{cases} \quad (7)$$

Smooth trajectories reaching high values for the acceleration of the trap centre for a short time seem hence to be favoured. This is confirmed by the results of Fig. 8(b), described in Appendix C. The limit of this strategy comes from the tilt of the potential in the comoving frame: above a certain value of the acceleration the atoms get anti-trapped resulting in large atom losses.

In order to estimate the heating of the gas due to the magnetic transport, we have measured the temperature

T of the cloud with a time of flight expansion. Relying on a model described in Appendix E, we are able to extract T from single shot data. We then normalize the results with the temperature of a gas at rest in the trap for the same total duration $2\Delta t$. This leads to the ratio r_T^2 presented in Fig. 4(c). Heating is observed for the shortest durations where r_T^2 starts to decrease significantly. The error function time profile gives the best results in particular for the shortest durations. Note that our clouds aren't at thermal equilibrium right after the loading of the magnetic trap. Since the collision rate in the trap is low (see Appendix D) the gas barely reaches thermal equilibrium even for the longest transport durations. Because of this, the temperature we extract from our data is strictly speaking an effective temperature and can be different along the horizontal and vertical direction. Nevertheless, our estimation of r_T^2 should still be accurate. Throughout the paper, r_T^2 is estimated from temperature fits along the horizontal direction.

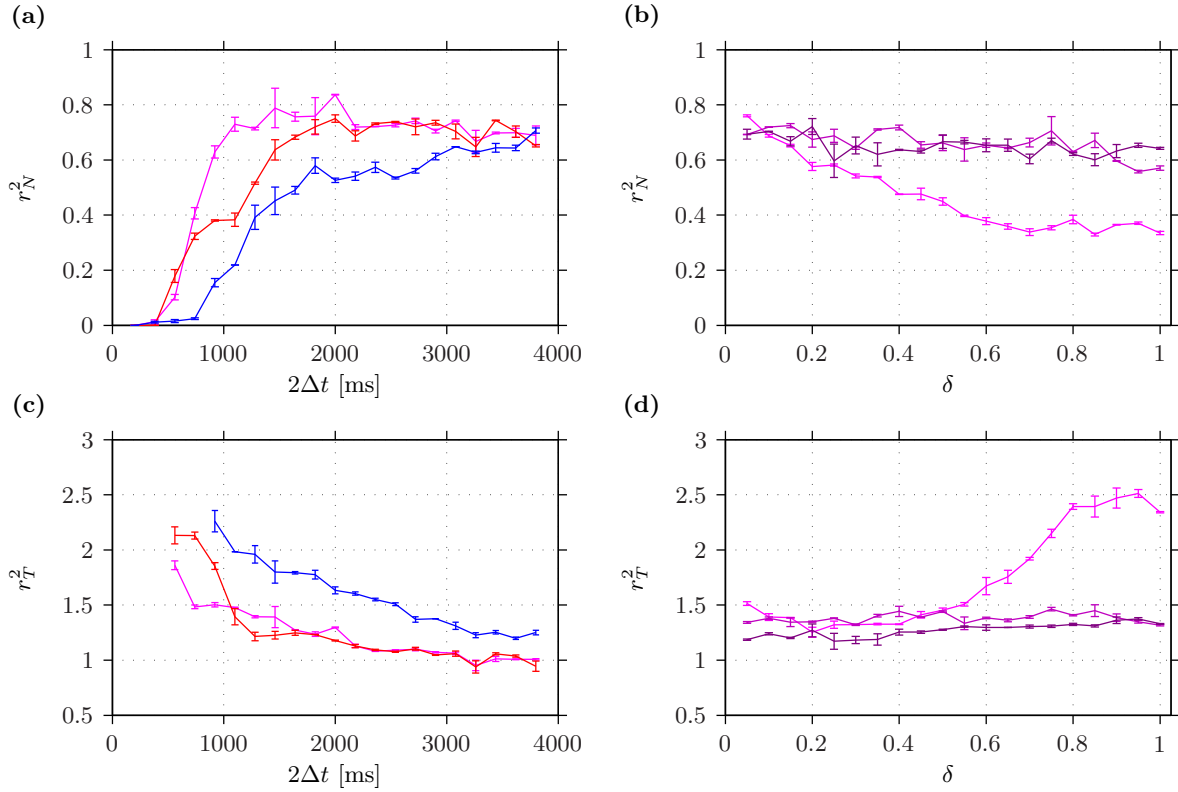


FIG. 4. (a) Ratio r_N^2 of the number of atoms remaining in the magnetic trap after a round trip along the first stage of the magnetic transport for different duration Δt and different time profiles: constant velocity (blue solid line), constant acceleration (red solid line) and error function shape with $\delta = 0$ (magenta solid line). (b) Ratio r_N^2 of the number of atoms remaining in the magnetic trap after a round trip along the first stage of the magnetic transport for the error function time profile with different values of δ and different Δt : 500 ms (magenta solid line), 750 ms (darker magenta solid line) and 1000 ms (darkest magenta solid line). (c),(d) Same as (a),(b) for the temperature ratio r_T^2 .

IV. CLASSICAL SIMULATIONS

Two loss sources can be considered in order to explain our observations: first, losses due to the finite depth of the magnetic trap. Second, Majorana losses due to the fact that the atomic spins cannot adiabatically follow the changes in the magnetic field orientation [15]. In this section we simulate classical trajectories of the atoms in the moving trap in order to compare different loss types for the different time profiles.

Considering each atom as a classical point-like particle, the equation of motion for each atom reads

$$m \frac{d^2 \mathbf{r}_a}{dt^2} = -\nabla V(y_0(t), t) \quad (8)$$

where $\mathbf{r}_a(t) = (x_a(t), y_a(t), z_a(t))$ is the position of an atom at time t and the potential V is fully determined by the three parameters b' , $\alpha(y_0)$ and $y_0(t)$. In the following, $b' = 65$ G/cm and $\alpha(y_0)$ follow the profile depicted in Fig. 2(b) as in the experiment. The trap centre trajectory, $y_0(t)$, follows either a constant velocity (Eq. 4), a constant acceleration (Eq. 5) or an error function with $\delta = 0$ (Eq. 7) time profile. As a reference, we have also

computed atomic trajectories in a static potential V with parameters $b' = 65$ G/cm, $\alpha(0) = 1$ and $y_0(t) = 0$.

With our typical atom number and temperature, the collision rate of the atoms in the trap is smaller than 1 s^{-1} (see Appendix D). To keep the treatment as simple as possible, in the following, we don't take into account interatomic interactions. Despite this choice, we expect our main conclusions to remain qualitatively valid thanks to the low collision rate experienced by the atoms.

In order to estimate the phase-space density of the gas throughout the magnetic transport, we have simulated 1000 different atomic trajectories indexed by parameter i , with initial positions $\mathbf{r}_a^i(t) = (x_a^i(0), y_a^i(0), z_a^i(0))$ randomly picked in order to reproduce a system initially at thermal equilibrium with temperature $T = 100 \mu\text{K}$ in the static trap V with parameters $b' = 65$ G/cm, $\alpha(0) = 1$ and $y_0(0) = 0$. This allows us to introduce a length scale $r_0 = k_B T / (g f m_F \mu_B b')$, with k_B the Boltzmann constant, and a velocity scale $v_0 = \sqrt{k_B T / m}$. The length r_0 is related to the size of the atomic cloud at rest while the velocity v_0 is simply the width of the velocity distribution along each direction of space.

In order to estimate finite depth losses in the trap associated to each time profile, we have computed for

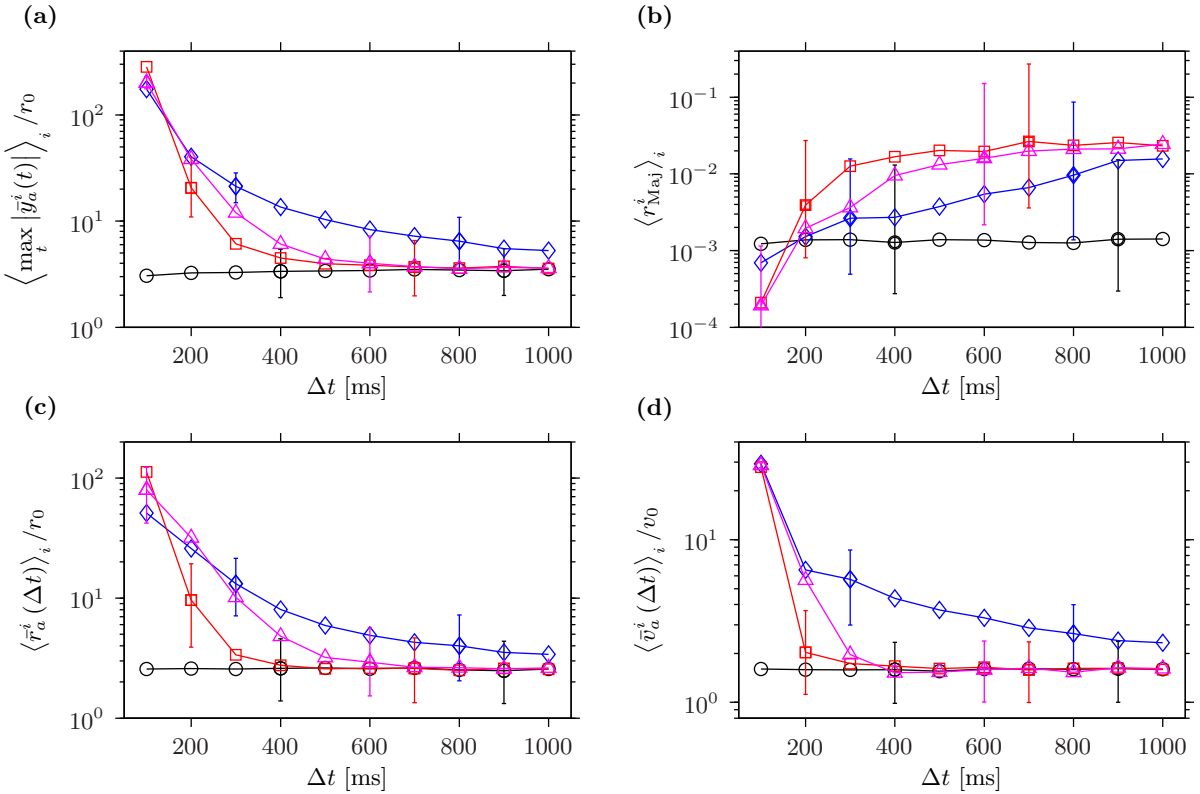


FIG. 5. (a) Mean value, deduced from the distribution, of maximal distances to the trap centre along the y axis for a given duration, Δt , and for constant velocity (blue diamonds), error function (magenta triangles), constant acceleration (red squares) and static trap (black circles). The error bars indicate the width of the distribution. Note that we take into account the potential asymmetry of the distribution on both sides of the mean and only two error bars per transport shape have been included, for clarity. (b) Same as in (a) but for the Majorana ratio (see text). (c) Same as (a) for the distance to the trap centre at the end of the magnetic transport. (d) Same as (a) for the velocity in the comoving frame at the end of the magnetic transport.

each trajectory i the maximal distance to the trap centre along the y axis $\max_t |\bar{y}_a^i(t)|$ where $\bar{y}_a^i(t) = y_a^i(t) - y_0(t)$.

Fig. 5(a) shows the mean value of this distribution for different transport duration Δt . The error bars indicate the width of the distribution. We observe that the error function and constant acceleration time profile results converge to the static potential ones as soon as $\Delta t > 500$ ms. The constant velocity time profile leads to trajectories which explore a significantly larger space around the trap centre. In our simulations, the potential is idealized and the trap depth is infinite. The atoms are never lost. This is not the case in the experimental realization of V , where the radius of the magnetic coils fixes an upper limit to the maximal distance to the trap centre. From the simulations we can then qualitatively expect a larger loss rate due to the finite depth of the trap for the constant velocity time profile than for the other two. The same analysis along the x and z direction gives similar results but with smaller maximal distances to the trap centre.

Estimating losses associated to Majorana spin flips requires the comparison of two frequencies: the rate associated with changes in the orientation of the magnetic

field $\nu_B^i(t) = \left\| \frac{d}{dt} \left\{ \frac{\mathbf{B}[\mathbf{r}_a^i(t), t]}{\|\mathbf{B}[\mathbf{r}_a^i(t), t]\|} \right\} \right\|$ and the Larmor frequency $\nu_L^i(t) = g_F m_F \mu_B \|\mathbf{B}[\mathbf{r}_a^i(t), t]\| / \hbar$. Defining the ratio $r_{\text{Maj}}^i = \max_t \nu_B^i(t) / \nu_L^i(t)$ we can compare the features of the distribution of r_{Maj}^i for the different time profiles. As soon as r_{Maj}^i gets close to 1, the probability of spin flip is high. In Fig. 5(b) we show that constant velocity trajectories lead on average to smaller values of r_{Maj}^i compared to constant acceleration or error function time profiles. This is explained by the larger extension of the trajectories towards larger magnetic fields and should qualitatively translate into a smaller loss rate associated with Majorana spin flips. Faster magnetic transport also leads to smaller r_{Maj}^i . We finally observe that all time profiles lead to larger values of r_{Maj}^i compared to the static case. This probably explains why the magnetic transport efficiency is never 100% even for the longest Δt in our experimental data.

In order to estimate the heating induced by the different time profiles we have calculated the distribution of distances to the trap centre at the end of the magnetic transport $\bar{r}_a^i(\Delta t)$ where $\bar{r}_a^i(t) =$

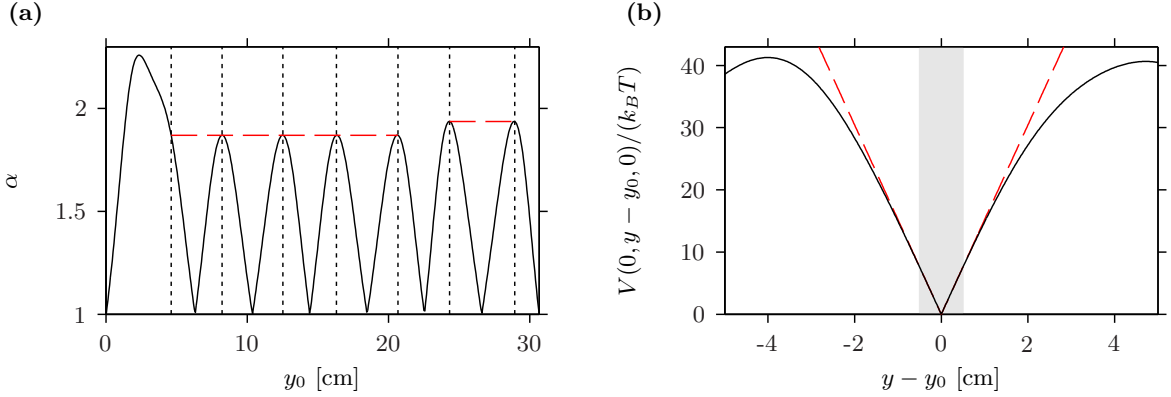


FIG. 6. (a) Dependence of α on the centre position of the magnetic quadrupole trap, y_0 , when only two consecutive pairs of anti-Helmholtz coils are used. The vertical dotted lines indicate the switching positions from one set of three pairs of anti-Helmholtz coils to the next (see text). The red dashed lines connect the maxima of α . (b) Cut in the magnetic quadrupole potential along the y axis around $y_0 = L_1/2$. The red dashed line corresponds to the approximate V of Eq. 3 with $b' = 65$ G/cm and $\alpha(y_0) = 1.87$. The black line corresponds to the analytical formula of V which takes into account the details of the geometry of each coil. The current flowing in the coils have been adjusted so that the black lines optimally fits the red dashed line within the light grey area (see text).

$\sqrt{(x_a^i(t))^2 + (y_a^i(t) - y_0(t))^2 + (z_a^i(t))^2}$. We have also computed the velocity distribution $\bar{v}_a^i(\Delta t)$ where $\bar{v}_a^i(t) = \sqrt{\left(\frac{dx_a^i}{dt}\right)^2 + \left(\frac{dy_a^i}{dt} - \frac{dy_0}{dt}\right)^2 + \left(\frac{dz_a^i}{dt}\right)^2}$. The mean value of the distribution for a given Δt is displayed in Fig. 5(c) and (d). The error bars indicate the width of the distribution. Constant velocity time profiles lead to larger mean distances and mean velocities than any other time profiles. The widths of the distributions follow the same behaviour. This can be seen as a signature of larger heating. For the constant acceleration and error function time profiles, the heating should be negligible as soon as $\Delta t > 600$ ms. These results agree qualitatively well with our experimental observations.

Overall, these simulations tend to indicate that the error function time profile realizes a trade-off between the two sources of losses we have identified. This is in good qualitative agreement with our experimental results and is probably sufficient to explain why the error function time profile leads to the best magnetic transport efficiency.

V. CONCLUSION

Comparing different time profiles, we have identified an efficient trajectory for the centre of a quadrupole trap designed for the transport of cold sodium ^{23}Na atoms. It relies on a smooth profile parametrized by the error function. Relying on classical simulations of individual trajectories of the atoms during the transport, we have been able to qualitatively investigate our experimental results: two main loss sources - finite depth of the trap and Majorana spin flips - limit the efficiency of the magnetic transport for the shortest durations. Constant velocity

trajectories tend to minimize the amount of Majorana spin flips while constant acceleration ones optimize the finite trap depth losses. Faster magnetic transport also tends to minimize Majorana losses while finite trap depth becomes a bigger limitation for all time profiles. The error function trajectory corresponds to a trade-off between these two types of losses with a sharp but finite acceleration at the beginning and the end of the transport and an almost constant velocity in between. Overall, we are able to transport on the order of $\sqrt{70\%} \approx 85\%$ of the atoms over the first stage of the magnetic transport (nearly 30 cm) in about 600 ms with limited heating of the gas. We have also tested that the same results could be obtained along the beginning of the second stage of the magnetic transport.

While this work doesn't answer the question of what is theoretically the optimal trajectory to transport cold atoms in a quadrupole trap over large distances, it gives good hints of the direction where to look for. We hope this will contribute to stimulate theoretical works relying on optimal control to determine the best transport trajectories in linear traps.

Appendix A: Experimental details

The different coils are made of flat copper wires of rectangular cross section $1 \times 2.5 \text{ mm}^2$. They are insulated with a thin Kapton® layer. The MOT and C_l coils, $l \in [1, 12]$, are made of 2 layers of 22 windings with outer and inner diameters of 72 mm and 26.6 mm respectively. Each C_{13} coil is made of 5 C_l coils soldered on top of each other. Each magnetic trap coil (MT) is made of 2 coils soldered on top of each other with 2 layers of 27 windings with an inner diameter of 124 mm. The push coil is conical and made of 16 layers with windings from

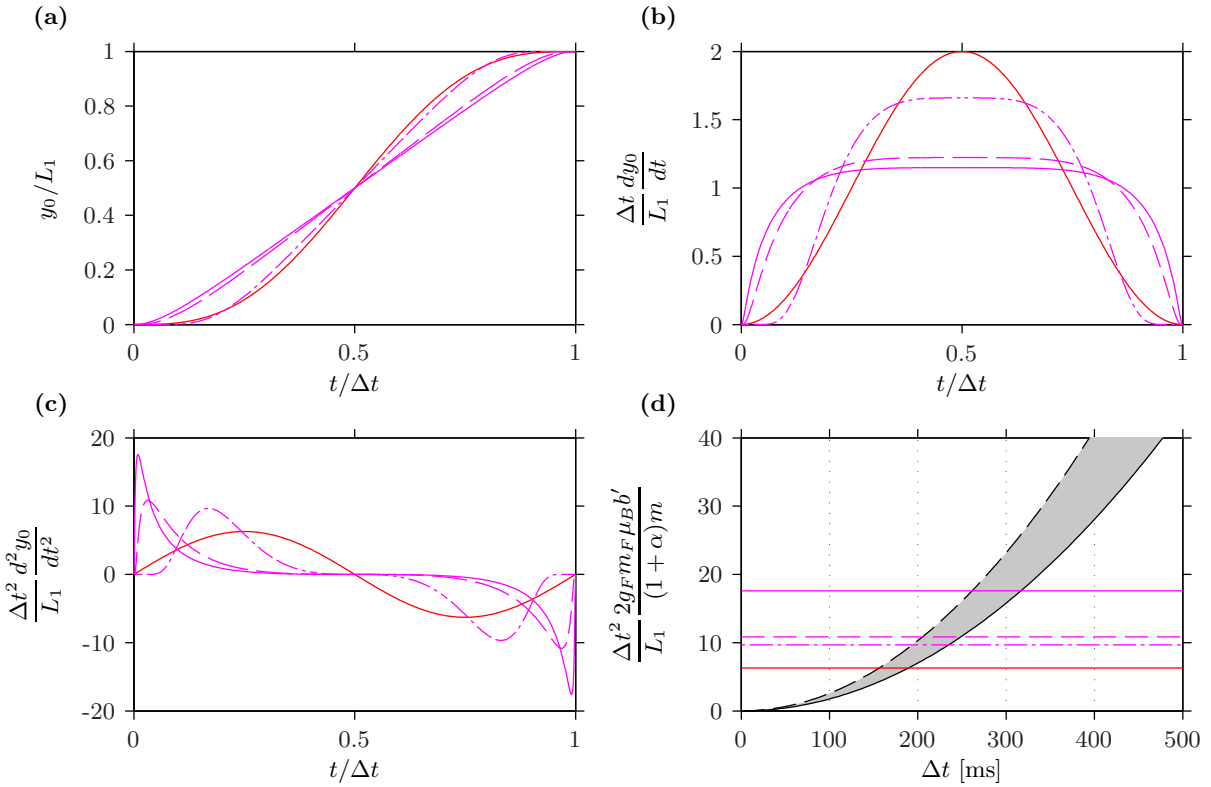


FIG. 7. (a) Behaviour of y_0 for different time profiles: sinusoidal acceleration (red solid line), hyperbolic tangent function shape (magenta lines): $\delta = 0.2$ (solid), $\delta = 0.3$ (dashed) and $\delta = 0.9$ (dashed-dotted). (b) Same as (a) for the velocity of the trap centre. (c) Same as (a) for the acceleration of the trap centre. (d) Absolute value of the acceleration corresponding to the slope of the potential V in units of $L_1/\Delta t^2$: $b' = 65$ G/cm and $\alpha = 1.937$ (black solid line) and $\alpha = 1$ (black dashed line). The grey shaded area indicates the range of slopes covered during the trajectory. The three horizontal magenta lines correspond to the maximal absolute value of the acceleration in unit of $L_1/\Delta t^2$ of the hyperbolic tangent function shape time profiles: $\delta = 0.2$ (solid line), $\delta = 0.3$ (dashed line) and $\delta = 0.9$ (dashed-dotted line). The horizontal red line is the same quantity for the sinusoidal acceleration profile.

2 to 16 and an inner diameter of 38 mm. Except for the latter, all the coils are mounted in a water-cooled aluminium frame.

Three current supplies (one SM 15-100 and two SM 60-100 models from DELTA ELECTRONIKA) are used to deliver the currents in the different coils. An electronic box relying on MOSFETs allows to quickly switch from one pair of coils to another one. The open/close sequences can be read from a rewritable component of the box, or they can be delivered as digital signals by an ADwin-Pro II system with a clock period of 4 μ s. The latter also provides the analog signals setting the output current of the different supplies at all time steps.

Appendix B: Determination of the currents

In order to determine the positions where we switch from one set of three pairs of anti-Helmholtz coils to the next, we first considered a situation where we only use two pairs of anti-Helmholtz coils to move the atoms. Fixing $b' = 65$ G/cm, we fit the currents of the two pairs of

anti-Helmholtz coils which lie on both sides of y_0 . This has the advantage of leading to positive current solutions only. If y_0 corresponds to the position of the symmetry axis of a given pair, the current in the other pair has to be zero and $\alpha(y_0) = 1$. As shown in Fig. 6(a), between two of these spots, α reaches a maximum: $\alpha = 1.87$ for the second to the fifth maximum, and $\alpha = 1.937$ for the sixth and seventh. These positions of maximal α are the ones we use in our design to switch from one set of three pairs of anti-Helmholtz coils to the next due to the fact that adding a third pair of anti-Helmholtz coils to adjust the shape of the quadrupole trap V can only lead to an increase of α if we restrict ourselves to positive currents. This is actually the opposite with the push coil for which the current direction is set so that positive currents in the push coil lead to lower values of α . This is why the first switching position in Fig. 6(a) is set where $\alpha = 1.87$, as in the next ones, and not to the maximum value of α reached with these two pairs of anti-Helmholtz coils.

In order to adjust the shape of the quadrupole trap V throughout the magnetic transport, we fit the analytical formula for V discussed in section II to the approximate

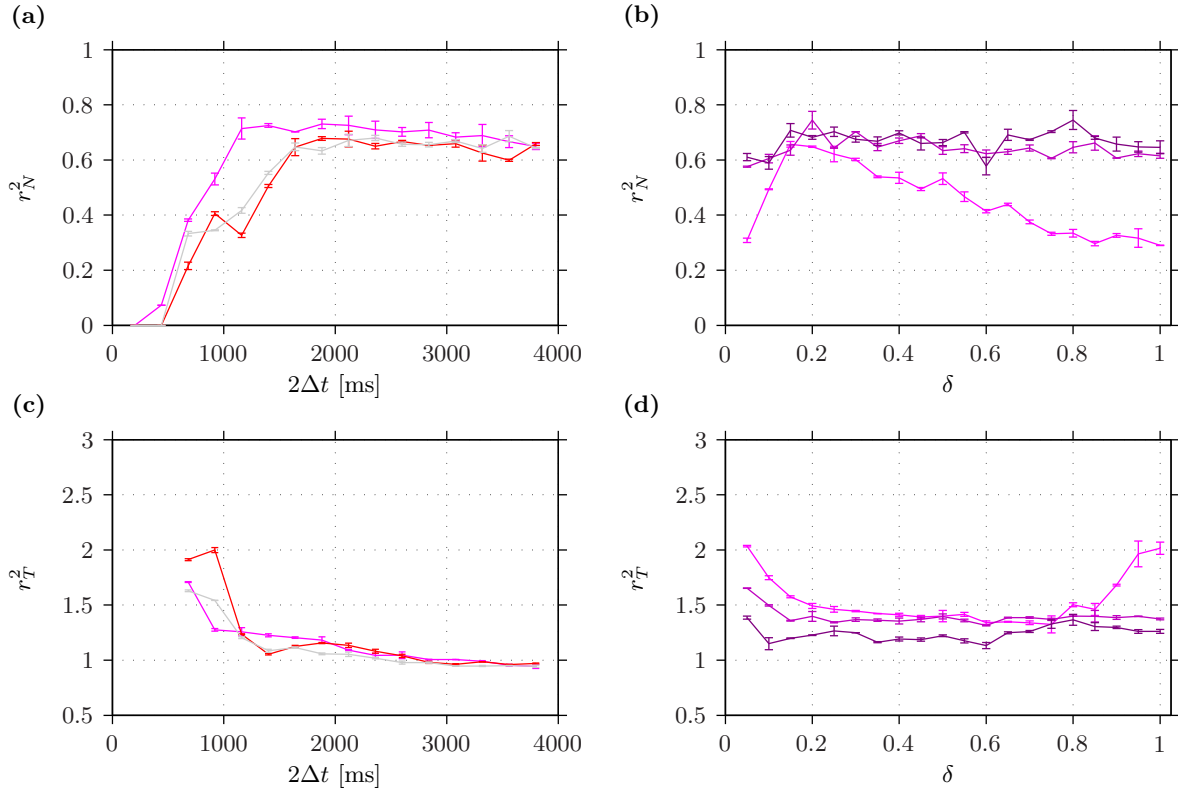


FIG. 8. (a) Ratio r_N^2 of the number of atoms remaining in the magnetic trap after a round trip along the first stage of the magnetic transport for different duration, Δt , and different time profiles: sinusoidal acceleration (red solid line), constant acceleration (grey solid line) and hyperbolic tangent function shape with $\delta = 0.3$ (magenta solid line). (b) Ratio r_N^2 of the number of atoms remaining in the magnetic trap after a round trip along the first stage of the magnetic transport for the hyperbolic tangent function time profile with different values of δ and different Δt : 500 ms (magenta solid line), 750 ms (darker magenta solid line) and 1000 ms (darkest magenta solid line). (c),(d) Same as (a),(b) for the temperature ratio r_T^2 .

profile given by Eq. 3 with $b' = 65$ G/cm and $\alpha(y_0)$ following the red dashed profile in Fig. 2(b). More precisely we compute $V(x, y_0, 0)$, $V(0, y_0 + y, 0)$ and $V(0, y_0, z)$ for $x, y, z \in [-5 \text{ mm}, 5 \text{ mm}]$ with a spatial grid of 101 points along each direction and rely on a least square algorithm to minimize the distance between the potential obtained by the analytical formula and the one deduced from Eq. 3. The currents in the three supplies are the only free parameters here. For the last few centimetres of the transport, only two current supplies are used and only the profile of V along the (Oz) axis is used. A typical result is illustrated in Fig. 6(b).

Appendix C: Other examples of trajectories

We have tested a few additional trajectories in order to complete our experimental observations presented in section III B. Their respective behaviours is shown in Fig. 7. The first time profile realizes a sinusoidal profile for the

acceleration:

$$\begin{aligned} y_0(t) &= 0 \quad t \leq 0 \\ y_0(t) &= L_1 \left[\frac{t}{\Delta t} - \frac{1}{2\pi} \sin \left(2\pi \frac{t}{\Delta t} \right) \right] \quad 0 < t < \Delta t \\ y_0(t) &= L_1 \quad t \geq \Delta t. \end{aligned} \quad (C1)$$

Such trajectory allows us to check whether the abrupt change in the acceleration in the constant acceleration time profile is critical or not. Fig. 8(a) actually shows that the answer is negative since it is hard to distinguish the performances of the two time profiles.

We have also tested a time profile very similar to Eq. 7 but replacing the error function by a hyperbolic tangent:

$$\begin{aligned} y_0(t) &= 0 \quad t \leq 0 \\ y_0(t) &= \frac{L_1}{2} \left\{ 1 + \tanh \left[-\gamma \left(\frac{t}{\Delta t} \right)^{-\delta} + \gamma \left(1 - \frac{t}{\Delta t} \right)^{-\delta} \right] \right\} \quad 0 < t < \Delta t \\ y_0(t) &= L_1 \quad t \geq \Delta t. \end{aligned} \quad (C2)$$

Such trajectory converges toward a constant velocity time profile when δ tends to zero. In Fig. 8(b), we observe

an optimum around $\delta \simeq 0.2$ for short values of Δt . This is in agreement with Fig. 7(d), where we qualitatively see that for $\delta > 0.2$ the duration Δt must be larger than 500 ms so that the atoms remain trapped throughout the transport.

Appendix D: Collision rate

The collision rate γ_c can be defined as [18]

$$\gamma_c = \langle n \rangle \langle v_r \rangle \sigma \quad (\text{D1})$$

where $\langle n \rangle$ is the mean density in the trap V , $\langle v_r \rangle$ the average relative collision velocity and $\sigma = 8\pi a^2$ the scattering cross-section with a the scattering length. The scattering length for sodium atoms in the $|F = 1, m_F = -1\rangle$ Zeeman substate is $a = 2.75$ nm [19]. For a cloud at thermal equilibrium in the trap V with $\alpha = 1$, one finds

$$\langle n \rangle = \frac{N}{32\pi r_0^3} \quad \langle v_r \rangle = \frac{4}{\sqrt{\pi}} v_0 \quad (\text{D2})$$

where N is the total atom number in the trap.

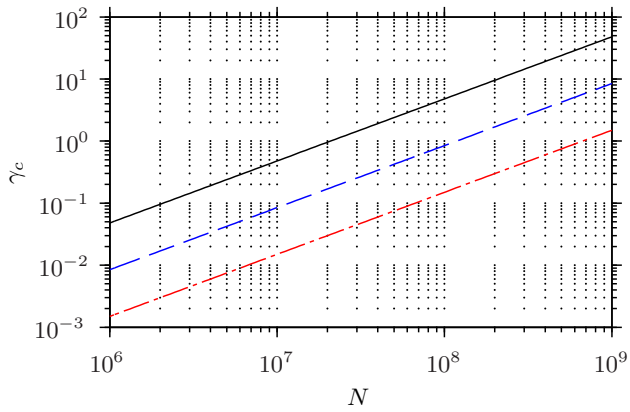


FIG. 9. Collision rate γ_c in the quadrupole magnetic trap V with parameters $b' = 65$ G/cm and $\alpha = 1$ for different atom number N and for a temperature $T = 50$ μK (black solid line), $T = 100$ μK (blue dashed line) and $T = 200$ μK (red dashed-dotted line).

We show in Fig. 9 how γ_c depends on N . For our typical atom number and temperature, $\gamma_c \lesssim 1 \text{ s}^{-1}$. This is in good qualitative agreement with our experimental observations of the thermalization time of our gas after loading into the magnetic quadrupole trap which is on the order of a few seconds, where $\sim 3\gamma_c^{-1}$ is expected from numerical simulations [18].

Appendix E: Thermometry

We estimate the temperature of the trapped gas by relying on a fit of the density profile of the atoms after a time of flight t_{tof} . If we assume the atoms to be initially at thermal equilibrium at a temperature T , the density in the quadrupole trap n is proportional to $\exp[-V/(k_B T)]$. More precisely, assuming $\alpha = 1$, we have

$$n(x, y, z) = \frac{N}{4\pi r_0^3} \exp\left[-\frac{\sqrt{x^2 + y^2 + 4z^2}}{r_0}\right]. \quad (\text{E1})$$

The velocity of the atoms \mathbf{v} simply follows a Maxwell-Boltzmann distribution

$$p(\mathbf{v}) = \frac{1}{(\sqrt{2\pi}v_0)^3} \exp\left(-\frac{\mathbf{v}^2}{2v_0^2}\right). \quad (\text{E2})$$

Neglecting interatomic collisions during the expansion of the gas, the density distribution after a time of flight t_{tof} stems from the free expansion of the atoms

$$n(\mathbf{r}; t_{\text{tof}}) = \frac{1}{t_{\text{tof}}^3} \int d\mathbf{u} n(\mathbf{u}) p\left(\frac{\mathbf{r} - \mathbf{u}}{t_{\text{tof}}}\right). \quad (\text{E3})$$

While Eq. E3 does not simplify into a simple analytical expression, integrating $n(\mathbf{r}; t_{\text{tof}})$ along the y and z axis leads to

$$n_{yz}(x; t_{\text{tof}}) = \frac{\beta_t N}{2\sqrt{2\pi}r_0} \exp\left(-\frac{x^2}{2\beta_t^2 r_0^2}\right) + \frac{N}{8r_0} \exp\left(\frac{\beta_t^2}{2}\right) \left[\exp\left(-\frac{x}{r_0}\right) \left(1 + \frac{x}{r_0} - \beta_t^2\right) \text{erfc}\left(\frac{\beta_t}{\sqrt{2}} - \frac{x}{\sqrt{2}\beta_t r_0}\right) + \exp\left(\frac{x}{r_0}\right) \left(1 - \frac{x}{r_0} - \beta_t^2\right) \text{erfc}\left(\frac{\beta_t}{\sqrt{2}} + \frac{x}{\sqrt{2}\beta_t r_0}\right) \right] \quad (\text{E4})$$

where $\beta_t = v_0 t_{\text{tof}}/r_0$ and erfc is the complementary error function. Integrating $n(\mathbf{r}; t_{\text{tof}})$ along the x and y axis leads to an expression for n_{xy} similar to Eq. E4 but where x has to be replaced by z , r_0 by $r_0/2$ and β_t by $2\beta_t$.

For long times of flight $\beta_t \gg 1$ and n_{xy} and n_{yz} both converge toward a simple Gaussian function with RMS width $\beta_t r_0 = v_0 t_{\text{tof}}$.

To experimentally measure the temperature of our

atomic clouds, we switch off the magnetic trap and let the atoms expand for a few milliseconds. Relying on absorption imaging along the y axis we obtain the integrated density profile $\int dy n(\mathbf{r}; t_{\text{tof}})$. Integrating numerically along either the x and z axis we can then fit the resulting profile with the analytical expression of n_{xy} or n_{yz} . This then gives us a measurement of the temperature of the cloud T in a single shot.

ACKNOWLEDGMENTS

We are grateful to D. Guéry-Odelin for helpful comments on the manuscript. We thank A. Kaladjian for the building of a large part of the mechanical pieces we have used for the fabrication of the coils and their mounts. This work has been supported by the ANR Project No. 11-PDOC-021-01 and the Région Île-de-France in the framework of DIM NanoK (Des atomes froids aux nanosciences) project FluoStrong. LPL is a member of DIM SIRTEQ (Science et Ingénierie en Région Île-de-France pour les Technologies Quantiques).

REFERENCES

- [1] M. Greiner, I. Bloch, T. W. Hänsch, and T. Esslinger, *Physical Review A* **63**, 031401 (2001).
- [2] W. Hänsel, J. Reichel, P. Hommelhoff, and T. W. Hänsch, *Physical Review Letters* **86**, 608 (2001).
- [3] W. Hänsel, P. Hommelhoff, T. W. Hänsch, and J. Reichel, *Nature* **413**, 498 (2001).
- [4] S. Minniberger, F. Diorico, S. Haslinger, C. Hufnagel, C. Novotny, N. Lippok, J. Majer, C. Koller, S. Schneider, and J. Schmiedmayer, *Applied Physics B: Lasers and Optics* **116**, 1017 (2014).
- [5] T. L. Gustavson, A. P. Chikkatur, A. E. Leanhardt, A. Görlitz, S. Gupta, D. E. Pritchard, and W. Ketterle, *Physical Review Letters* **88**, 020401 (2001).
- [6] D. Schrader, S. Kuhr, W. Alt, M. Müller, V. Gomer, and D. Meschede, *Applied Physics B: Lasers and Optics* **73**, 819 (2001).
- [7] A. Couvert, T. Kawalec, G. Reinaudi, and D. Guéry-Odelin, *EPL (Europhysics Letters)* **83**, 13001 (2008).
- [8] H. J. Lewandowski, D. M. Harber, D. L. Whitaker, and E. A. Cornell, *Journ. Low Temp. Phys.* **132**, 309 (2003).
- [9] S. Händel, A. L. Marchant, T. P. Wiles, S. A. Hopkins, and S. L. Cornish, *Review of Scientific Instruments* **83**, 013105 (2012).
- [10] T. Lahaye, G. Reinaudi, Z. Wang, A. Couvert, and D. Guéry-Odelin, *Physical Review A* **74**, 033622 (2006).
- [11] S. Schmid, G. Thalhammer, K. Winkler, F. Lang, and J. H. Denschlag, *New Journal of Physics* **8**, 159 (2006).
- [12] E. Torrontegui, S. Ibáñez, X. Chen, A. Ruschhaupt, D. Guéry-Odelin, and J. G. Muga, *Physical Review A* **83**, 013415 (2011).
- [13] Q. Zhang, X. Chen, and D. Guéry-Odelin, *Physical Review A* **92**, 043410 (2015).
- [14] Q. Zhang, J. G. Muga, D. Guéry-Odelin, and X. Chen, *Journal of Physics B: Atomic, Molecular and Optical Physics* **49**, 125503 (2016).
- [15] E. Majorana and M. Inguscio, in *Ettore Majorana Scientific Papers*, Vol. 9 (Springer, Berlin, Heidelberg, 1932) pp. 113–136.
- [16] T. Bergeman, G. Erez, and H. J. Metcalf, *Physical Review A* **35**, 1535 (1987).
- [17] D. Ben Ali, T. Badr, T. Brézillon, R. Dubessy, H. Perrin, and A. Perrin, *Journal of Physics B: Atomic, Molecular and Optical Physics* **50**, 055008 (2017).
- [18] J. Dalibard, in *Proceedings of the International School of Physics "Enrico Fermi" Volume 140 : Bose-Einstein Condensation in Atomic Gases*, edited by M. Inguscio, S. Stringari, and C. Wieman (Società italiana di Fisica, 1999) pp. 321–349.
- [19] E. Tiesinga, C. Williams, P. Julienne, K. Jones, P. Lett, and W. Phillips, *Journal of Research of the National Institute of Standards and Technology* **101**, 505 (1996).